

# Reconfigurable Millimeter-wave Reflectarray based on Low Loss Liquid Crystals

Dayan Pérez-Quintana, Erik Aguirre, Eduardo Olariaga, Sergei A. Kuznetsov, Valeri I. Lapanik, Vitaly S. Sutormin, Victor Ya. Zyryanov, Jose A. Marcotegui, and Miguel Beruete

**Abstract**—This paper reports on the development and evaluation of a reconfigurable millimeter-wave reflectarray based on liquid-crystal (LC) substrate operating in the D-band (105-125 GHz). The reflectarray is composed of a high-impedance surface with a meta-array of  $33 \times 29$  patches on a 2-mm-thick quartz substrate, separated from the ground plane by a 40  $\mu\text{m}$ -thick LC layer. A novel LC composition with low dielectric losses ( $< 0.003$ ) and high dielectric anisotropy ( $> 1.3$ ) has been developed for operation at millimeter-waves. The results demonstrate a reflection phase tunability of 210 degrees and low insertion losses of 2.5 dB. Furthermore, the device was demonstrated as a proof of concept for 1D beam-steering applications, exhibiting an operational bandwidth of 12 GHz.

**Index Terms**—Reconfigurable reflectarray, high impedance surfaces, liquid crystals, beam steering, D-band, millimeter waves.

## I. INTRODUCTION

RESEARCH on wireless communication systems has seen a rapid increase in recent decades, leading to the development of new technologies. Driven by the implementation of 5G, the emergence of 6G, and the IoT paradigm, wireless technology has undergone sustained evolution to meet the wider bandwidth requirements and higher operation frequencies. Smart antennas that can electronically steer beams are a crucial component in this revolution in wireless communications.

Reconfigurable or tunable reflectarray (RA) antennas have gained significant attention in recent years due to their ad-

vantages over conventional phased arrays. The integration of active elements such as PIN diodes and MEMS [1]–[4] has resulted in a reduction of physical size, as well as low cost and ease of integration. However, the manufacturing and integration challenges, as well as the parasitic effects at submillimeter waves, have limited their use in frequency bands above 50 GHz [5]. To fully utilize this frequency range, new techniques for dynamic control over the RA's electromagnetic response are needed.

Liquid crystals (LCs) offer a promising solution for the development of electronically reconfigurable/switchable RA antennas that operate at short millimeter and terahertz waves, without the mentioned drawbacks of current technology. LCs are a special aggregate state of matter with characteristics of both solids and liquids. Their uniaxial nature and the ability to rotate/align the molecules by applying an external biasing voltage or other techniques allow for tuning of the effective dielectric permittivity. Since their introduction [6], LCs have primarily been utilized in high-resolution displays (LCDs) [7] and optical frequency spatial light modulators [8]. Recent work [9] has demonstrated the potential of active LC-plasmonic metasurface in developing electrically switchable color tags, with a dynamic wavelength shift of greater than 100 nm at a low driving voltage (0-5 V), leading towards the possibility of next-generation dynamic optical devices.

One of the main challenges in using LCs for tunable devices at lower frequencies such as microwaves and millimeter waves is the contrast between the LC layer thickness (typically 2-10  $\mu\text{m}$ ) and the wavelength (in the centimeter and millimeter scale). When the radiation propagates perpendicular to the LC layer, this results in a weak wave-LC interaction, leading to minimal tuning of the response when the LC is modulated. Additionally, the values of the LC permittivity along the ordinary and extraordinary axes are not significantly different, which means that a large LC thickness is necessary to obtain significant phase differences at the output. However, a large thickness of the LC would require high external voltages to bias it properly, ultimately causing damage to the LC due to dielectric breakdown.

To overcome these limitations, resonant structures can be used to obtain LC-based tunable devices at microwaves, millimeter waves, and terahertz as reported in [5], [10], [11], [12]. The underlying mechanism is based on the property that the phase (in transmission or reflection) near a resonance undergoes a fast variation, leading to a steep slope in the frequency response. Intuitively, this fast variation can be interpreted as if the structure was made effectively larger.

Manuscript received XX; revised XX; accepted XX. Date of publication XX; date of current version XX. This work was supported This work was supported by MCIN/AEI/10.13039/501100011033/FEDER “Una manera de hacer Europa” via Project No. RTI2018-094475-B-I00. (Corresponding author: Miguel Beruete.)

Dayan Pérez-Quintana and Miguel Beruete are with the Antennas Group, Universidad Pública de Navarra, 31006 Pamplona, Spain, and also with the Institute of Smart Cities (ISC), Universidad Pública de Navarra, 31006 Pamplona, Spain (e-mail: dayan.perez@unavarra.es; miguel.beruete@unavarra.es).

Erik Aguirre is with the Institute of Smart Cities (ISC), Universidad Pública de Navarra, 31006 Pamplona, Spain and also TAFCO METAWIRELESS, S.L., 31013 Berriozar, Spain (e-mail: eaguirre@tafcomw.com).

Eduardo Olariaga and Jose A. Marcotegui are with TAFCO METAWIRELESS, S.L., 31013 Berriozar, Spain (e-mail: eolariaga@tafcomw.com; jmarcotegui@tafcomw.com).

Sergei A. Kuznetsov is with Novosibirsk State University, 630090 Novosibirsk, Russia (e-mail: sakuznetsov@nsu.ru).

Valeri I. Lapanik is with Institute of Applied Physical Problems, 220045 Minsk, Belarus (e-mail: valeri.lapanik@yahoo.com).

Vitaly S. Sutormin is with Kirensky Institute of Physics, Federal Research Center KSC SB RAS, Krasnoyarsk 660036, Russia and also with Siberian Federal University, Krasnoyarsk 660041, Russia (e-mail: sutormin@iph.krasn.ru).

Victor Ya. Zyryanov is with Kirensky Institute of Physics, Federal Research Center KSC SB RAS, Krasnoyarsk 660036, Russia (e-mail: zyr@iph.krasn.ru).

Hence, in the vicinity of the resonance, a modulation of the LC permittivity by rotating the LC molecules from the ordinary to the extraordinary axis or vice versa can lead to a significant phase difference at the output. In [13], LC unit cells operating in the X-band were analyzed. A tunable dynamic phase range of  $221^\circ$  was achieved over a band of 220 MHz (fractional bandwidth of 2.2%) using a K15 nematic LC. A similar strategy was exploited in [14], where a printed RA antenna was simulated and manufactured in the X-band. There, a reconfigurable monopulse-shaped radiation pattern was demonstrated using a metallic microstrip patch sitting on a  $500 \mu\text{m}$  cavity filled with a LC substrate by dynamically switching the permittivity of the LC substrate in the two halves of a RA aperture. In [15], a RA consisting of  $52 \times 54$  identical cells, each one composed of three parallel dipoles of different lengths placed on an LC substrate and operating in F-band was proposed. This design exhibited an 8% fractional bandwidth with moderate losses ( $\sim 7$  dB), using a low cost manufacturing process able to produce antennas in frequencies from 60 to 500 GHz. In [16] a particular configuration of a unit cell, composed of a microstrip patch was analyzed. Applying low frequency AC bias voltages of 10 V, a  $165^\circ$  phase shift with a loss between 4.5 and 6.4 dB at 102 GHz and  $130^\circ$  with similar losses at 130 GHz was demonstrated.

In this work, a reconfigurable RA with low losses and moderate bandwidth is implemented using a novel nematic LC composition. With an LC thickness of  $40 \mu\text{m}$ , this resonant structure was designed to operate in the frequency band of 105-120 GHz corresponding to an average wavelength/thickness ratio of 67 and to allow independent electric control of RA unit cells in one dimension (for 1D beam steering). This investigation introduces two key advancements: 1) the experimental verification of the low losses exhibited by the developed LC composition in meta-devices, and 2) the identification of an optimal RA configuration that strikes a balance between fabrication simplicity, precise phase control, moderate bandwidth, and harnessing the advantages of the new LC composition's low losses.

Hence, our experimental results underscore the groundbreaking capabilities of LC technology in the millimeter wave domain. We have successfully achieved precise beam guidance in the intended direction by utilizing an LC-based reconfigurable reflectarray. A pivotal aspect of this research was the development of a unique LC composition tailored exclusively for millimeter-wave applications. Our device demonstrates exceptional performance, with impressively low loss values of approximately 2.5 dB. This novel LC composition requires further testing and optimization to exploit its capabilities fully. Nonetheless, this investigation provides compelling evidence of LC crystals' immense technological potential in reconfigurable devices operating at millimeter waves.

This paper is organized as follows. In Section II, the operational principle of the design, along with its basic electromagnetic features, is described. Additionally, the proposed design and simulated electromagnetic response of the reconfigurable RA are presented. In Section III, the fabrication process of the RA prototype is outlined, and a detailed experimental study is conducted. The key findings and conclusions are summarized

in Section IV. Finally, the properties of the LC composition used in the study are discussed in an Appendix for the sake of completeness.

## II. DESIGN AND NUMERICAL RESULTS

### A. Operation Principle of the LC-based RA: the Role of High Impedance Surfaces

A LC-based reflectarray (RA) often presents a significant difference between the operating free-space wavelength  $\lambda$  and the LC layer thickness  $h_{LC}$ . Their electromagnetic properties can be understood through the concept of high-impedance surfaces (HIS) [18], also known as artificial magnetic conductors, which were originally introduced as ultra-thin substrates for low-profile antennas in the microwave antenna engineering community.

In a conventional design, a LC-loaded RA consists of a single-layered, capacitive frequency-selective surface or metasurface (MS) patterned on a thin dielectric slab (in this case, the LC layer, referred to as LC), with a uniform back metalization, i.e. a ground plane (GP). The MS impedance  $Z_{MS}$  in the RA operation frequency band must satisfy  $\Im(Z_{MS}) < 0$  for it to be considered capacitive. The thinnest HIS is achieved when the MS is composed of disconnected subwavelength metallic elements, such as patches [see Fig. 1(a)], operating at frequencies  $\omega$  below any possible plasmonic resonance,  $\omega < \omega_{res}$ . In the limit  $\omega \rightarrow 0$ , the metallic elements do not support surface currents and act as effective lumped capacitances  $C_{MS}$ :  $Z_{MS}|_{\omega \rightarrow 0} = 1/(j\omega C_{MS})$ .

When the LC thickness ( $h_{LC}$ ) is much smaller than the operation wavelength ( $h_{LC}/\lambda \ll 1$ , ultra-thin regime), and disregarding dissipative losses, the input impedance of the "grounded" LC layer becomes purely inductive [18]:

$$Z_{in} = jZ_{LC} \tan(\sqrt{\varepsilon_{LC}}k_0 h_{LC}) = j\omega L_{LC} \quad (1)$$

where  $\varepsilon_{LC}$  is the relative permittivity of the LC layer (for the moment in this analysis we are neglecting LC anisotropy for simplicity),  $Z_{LC}$  is the characteristic impedance of the LC layer and  $k_0$  is the free-space wavenumber. The term  $L_{LC}$  represents the effective inductance of the "grounded" layer, which, for ultrathin LC, is linearly proportional to its thickness  $h_{LC}$ :

$$L_{LC} \approx \mu_0 h_{LC} \quad (2)$$

where  $\mu_0$  is the free-space magnetic permeability and it has been assumed that the LC crystal has a negligible magnetic response at subTHz frequencies. The structure can then be modeled as a parallel connection of  $Z_{MS}$  and  $Z_{LC}$ , as shown in Fig. 1(b), forming a resonant circuit. In the lossless case with a purely capacitive MS, the total impedance  $Z$  is:

$$Z \cong \frac{j\omega L_{LC}}{1 - \omega^2 C_{MS} L_{LC}} \quad (3)$$

The reflection coefficient  $S_{11}$  can be obtained from the total impedance through the next well-known relation [19]:

$$S_{11} = \frac{Z - \eta_0}{Z + \eta_0} \quad (4)$$

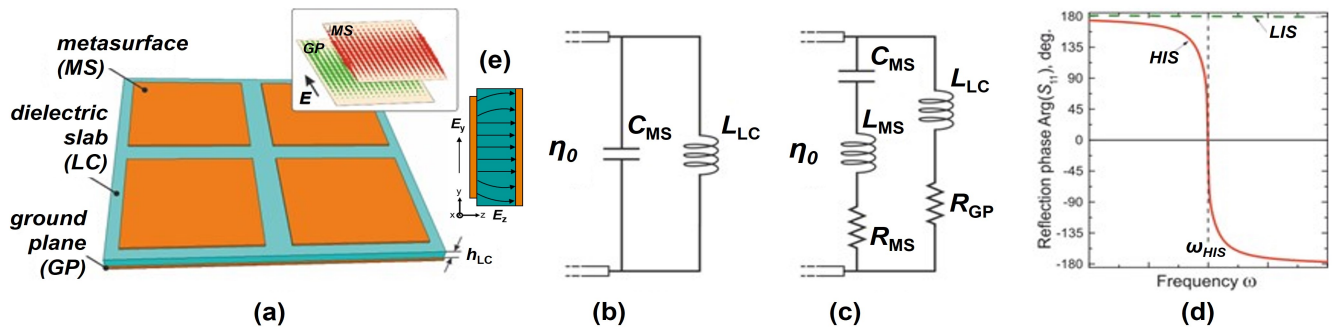


Fig. 1. Conventional HIS configuration (a) and its simplified (b) and complete (c) equivalent circuit representation. The lumped resistance  $R_{MS}$  is introduced to take into account ohmic dissipation in the MS metallization and dielectric losses in the LC layer, while  $R_{GP}$  describes ohmic dissipation in the GP [17]. (d) Qualitative spectral behavior for the HIS reflection phase. (e) Illustration of the vector distributions of surface currents induced in the MS and GP layers at the HIS resonance (full-wave simulations) and the electric field distribution lines in the LC.

The HIS resonance is achieved at the angular frequency  $\omega_{HIS} = 1/\sqrt{C_{MS}L_{LC}}$  where the total impedance goes to infinity. The typical spectral behavior of the reflection phase  $Arg\{S_{11}\}$  near the HIS resonance is shown in Fig. 1(d). As shown there,  $Arg\{S_{11}\}$  undergoes a strong variation near  $\omega_{HIS}$ , at which the phase is exactly equal to zero and then  $S_{11} = +1$ , as corresponds to an artificial magnetic conductor. Hence, the response of HISs is complementary to ordinary electric conductors (metals) that behave as low-impedance surfaces, for which  $S_{11} \cong -1$  which implies that  $|Arg(S_{11})| \cong 180^\circ$ . As illustrated in the inset in Fig. 1(e), the artificial magnetic properties of the HIS-structure originate from large antiparallel surface currents flowing in the MS and GP layers at the HIS resonance. These currents are induced almost in phase and form an effective magnetic dipole with a magnetic flux concentrated mainly between the MS and GP. The circuit is closed through displacement currents arising between the top patch and the bottom ground plane. This electric field associated to this capacitance is schematically sketched in Fig. 1(e).

From this figure it is clear that the capacitance strongly depends on the permittivity of the LC crystal. In particular, it will depend mainly on the LC tensor component parallel to the  $z$  axis. This fact along the rapid change of  $Arg\{S_{11}\}$  near resonance is crucial for the operation of the LC-loaded RA. Actually, the phase tunability of the RA is achieved by rotating the LC molecules by means of a biasing quasi-static external electric field, which, in essence, varies the effective permittivity seen along  $z$ , directly affecting the LC-loaded MS capacitance  $C_{MS}$ . A rapid change of  $Arg\{S_{11}\}$  is also important as it enhances the sensitivity to a variation of the permittivity.

In practical RA implementations, the biasing is achieved by using the top MS and GP as electrodes. In the case of a patch array MS, this is done by interconnecting the patches through thin inductive strips. Excitation of the structure is then achieved by applying an electric field perpendicular to these strips. Another option is to utilize a MS with an 'inductive' topology, characterized by a metal layer with slot-like resonant elements that operate at frequencies where the imaginary component of the impedance,  $\Im(Z_{MS})$ , is negative. In this case,

when the MS inductance  $L_{MS}$  cannot be neglected [Fig. 1(c)], the HIS resonance for the lossless regime ( $R_{MS} = R_{GP} = 0$ ) is achieved at the frequency [17], [20]:

$$\omega_{HIS} \cong \frac{1}{\sqrt{C_{MS}L_{LC}}} \left(1 + \frac{L_{MS}}{L_{LC}}\right)^{-1/2} \quad (5)$$

It is clear that the narrower the fractional HIS bandwidth  $\Delta\omega_{HIS}/\omega_{HIS}$ , the stronger the tunability. Derived from the definition  $|Arg\{S_{11}(\omega_{HIS} \pm 1/2\Delta\omega_{HIS})\}| = 90^\circ$  [17], under the condition  $\omega_{HIS}L_{LC} \ll \eta_0$ , the bandwidth is bound to the  $h_{LC}/\lambda_{HIS}$  ratio via a weakly non-linear law [17], [20]:

$$\begin{aligned} \frac{\Delta\omega_{HIS}}{\omega_{HIS}} &\cong \frac{1}{\eta_0} \sqrt{\frac{L_{LC}}{C_{MS}}} \left(1 + \frac{L_{MS}}{L_{LC}}\right)^{-3/2} \\ &= 2\pi \left(1 + \frac{c_0 L_{MS}}{\mu\eta_0 h_{LC}}\right)^{-1} \frac{h_{LC}}{\lambda_{HIS}}. \end{aligned} \quad (6)$$

Relation (6) illustrates the key feature of the HIS configuration: the bandwidth is proportional to the thickness of the structure. A supplementary conclusion arising from (6) is that the bandwidth can be additionally decreased by increasing the MS inductance  $L_{MS}$  (see also [17]).

### B. RA Unit Cell Design

The unit cell of the proposed RA has a width  $d_x = 0.9$  mm and a height  $d_y = 1.05$  mm, as depicted in Fig. 2. The structure consists of two quartz wafers, of thickness 2 and 6 mm respectively, represented in red. Quartz was selected due to its low dielectric losses in the frequency range of interest, as discussed below. The LC material, depicted in cyan, is deposited between both wafers and has a height of  $40 \mu\text{m}$  ( $h_{LC} = 40 \mu\text{m}$ ). The MS is patterned on the bottom surface of the 2 mm quartz wafer, laying over the LC substrate. The MS unit cell consists of a rectangular aluminum patch with transverse dimensions  $w_x = 0.65$  mm and  $w_y = 0.08$  mm and thickness  $t = 0.4 \mu\text{m}$  connected through narrow strips  $70 \mu\text{m}$ -wide to the vertically neighboring unit cells (represented in orange), which serve to distribute the same electric potential to all patches for LC biasing. The lower electrode is composed

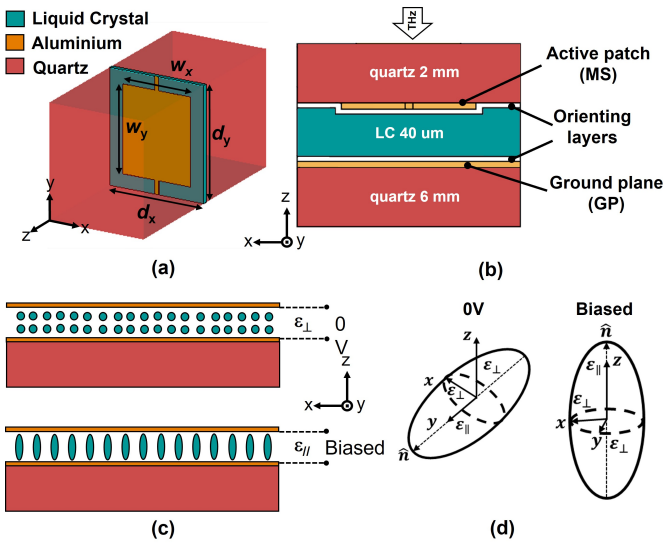


Fig. 2. Schematic view of the LC-based RA unit cell: (a) isometric view with the main dimensions; (b) cross-sectional view, showing the materials and arrangement. (c) Schematic representation of the LC molecules in the 0 V and biased states. (d) LC permittivity tensor orientation in both states.

of a uniform, 0.4  $\mu\text{m}$ -thick aluminum layer, serving as the GP bottom electrode, and held at a zero potential.

As shown in Fig. 2(b), two thin orienting layers are deposited onto both the MS and GP. They are made of poly(vinyl alcohol) and have a subwavelength thickness ( $\leq 0.1 \mu\text{m}$ ) so they have negligible impact on the electromagnetic response of the device. These orienting layers are crucial in LC technology as they ensure proper alignment of the LC molecules through a mechanical rubbing process. In the present design, the LC molecules are aligned parallel to the  $y$ -axis when no bias voltage is applied.

### C. RA Full-Wave Simulations

All the full-wave simulations in this work were performed using the commercial electromagnetic software CST Microwave Studio® [21]. Aluminum was modeled as a lossy metal with conductivity  $\sigma = 3.56 \times 10^7 \text{ S/m}$ , and quartz as a dielectric with a complex relative permittivity  $\epsilon_{\text{Quartz}} = 3.78(1 - j0.002)$ .

The inherently anisotropic LC medium was modeled using a complex dielectric permittivity tensor  $\bar{\epsilon}$ . In general, the local components of  $\bar{\epsilon}$  at every point of the LC layer depend on the orientation of the local director vector of LC molecules. This vector is the local optical axis of each LC molecule and is a function of the local bias electric field inside the medium. Since the biasing of the LC is done by applying a low-frequency AC voltage (typically 1 kHz) [22], in a strict sense, an accurate electromagnetic analysis of the RA should involve two subsequent stages: 1) calculation of the 3D spatial distribution of the quasi-static electric field inside the LC cell to get the geometrical distribution of local directors taking into account the geometry of the MS electrode (with an AC bias voltage as a variable parameter); 2) full-wave high-frequency simulations of the RA response at millimeter-waves using

the 3D spatial distribution of the dielectric permittivity tensor  $\bar{\epsilon}(x, y, z)$  obtained from the previously calculated LC director distribution. This two-stage scheme for the electromagnetic analysis of LC devices is non-trivial and is not directly implemented in commercial electromagnetic simulators. In a recent work [11], an analytical method is proposed to solve this problem. The dynamic differential equation governing the LC performance under different bias states is solved exactly by combining a finite-element software (COMSOL) and a full-wave electromagnetic analysis tool (CST). This comprehensive method is fully justified for complex unit cells comprising several elements such as the one discussed in [11]. In our case, given the simple geometry of the considered unit cell, this problem can be solved approximately by assuming that the LC director is rotated uniformly below the upper patch as the biasing voltage is varied and is kept with the original orientation (parallel to  $y$ ) outside the patch. This assumption is reinforced by the good agreement with the experimental results presented in Section III.

TABLE I  
DIELECTRIC PROPERTIES OF THE EMPLOYED LC.

$\epsilon'_{\perp}$	$\epsilon'_{\parallel}$	$\Delta\epsilon'$	$\tan\delta_{\perp}$	$\tan\delta_{\parallel}$
2.47	3.25	0.78	0.003	0.002

The seed values of the dielectric permittivity tensor of the LC substrate were extrapolated from the results for the frequency range of 27.5-29 GHz presented in [23] and were subsequently optimized and fitted to the measurement results (see Section III) leading to the optimal values summarized in I. The optimization developed was a multi-objective process provided by the CST Microwave Studio®. The values of the real part  $\epsilon_{\perp, \parallel}$  and loss tangent  $\tan\delta_{\perp, \parallel}$  of the complex relative dielectric permittivity  $\epsilon_{\perp, \parallel} = \epsilon'_{\perp, \parallel}(1 - j \tan\delta_{\perp, \parallel})$  parallel and perpendicular to the vector of the high-frequency electric field, respectively, are presented in Table. I (see Appendix)

In the implemented electromagnetic model, the orientation of the LC director vector  $\hat{n}$  was specified by the angle  $\alpha$  counted from  $y$ -axis in  $yz$ -plane:  $\hat{n} = (0, \cos\alpha, \sin\alpha)$ . In the unbiased state ( $V_b = 0$ ) the LC molecules are oriented along the rubbing direction, i.e.  $y$ -axis [ $\alpha = 0$ , Fig. 2(c), top and (d) “0 V”], and the permittivity tensor in the chosen coordinate system  $xyz$  has a diagonal form [24]:

$$\bar{\epsilon}(V_b = 0) = \begin{bmatrix} \epsilon_{\perp} & 0 & 0 \\ 0 & \epsilon_{\parallel} & 0 \\ 0 & 0 & \epsilon_{\perp} \end{bmatrix} \quad (7)$$

Likewise, in the maximum bias state the LC director is oriented perpendicular to the wafer surface, i.e. along  $z$ -axis [ $\alpha = 90 \text{ deg}$ , Fig. 2(c), bottom and (d) “Biased”], and the permittivity tensor transforms to:

$$\bar{\epsilon}(V_b = V_{max}) = \begin{bmatrix} \epsilon_{\perp} & 0 & 0 \\ 0 & \epsilon_{\perp} & 0 \\ 0 & 0 & \epsilon_{\parallel} \end{bmatrix} \quad (8)$$

To cover all possible intermediate orientations of the LC optical axis in the CST Microwave Studio® we introduced the local coordinate system  $x'y'z'$  associated with the LC

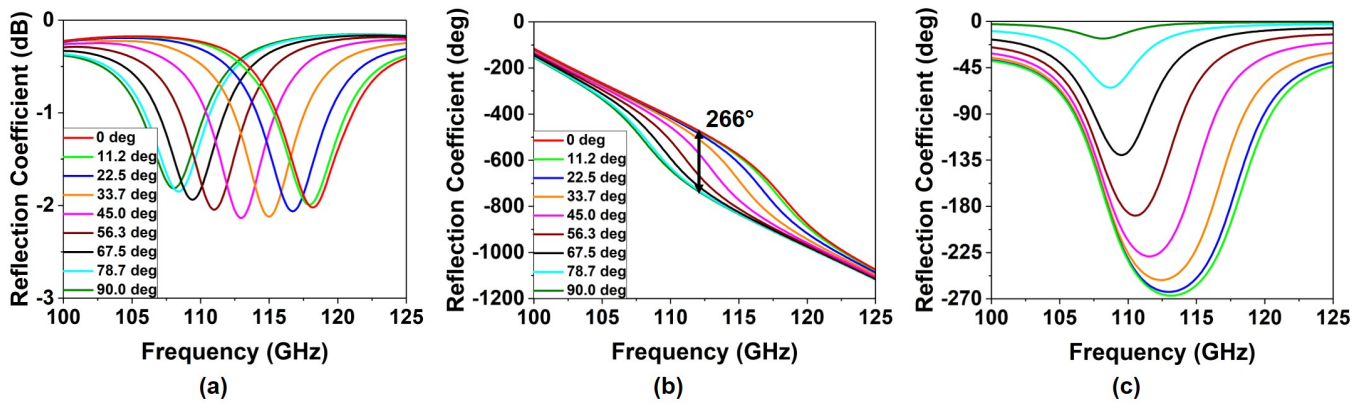


Fig. 3. Simulated characteristics of the RA for different orientation angles  $\alpha$  of the LC director: (a) reflection coefficient magnitude in dB; (b) reflection phase in degrees; (c) phase curves normalized to the case of 0 deg.

layer, in which the  $x'$ -axis coincides with the  $x$ -axis of the global coordinate system  $xyz$  and the  $y'$ -axis coincides with the LC director vector  $\hat{n}$ , respectively. The unit vector basis  $e_{x'}, e_{y'}, e_{z'}$  of the system  $x'y'z'$  is as follows:  $e_{x'} = (1, 0, 0)$ ,  $e_{y'} = (0, \cos \alpha, \sin \alpha)$ ,  $e_{z'} = (0, -\sin \alpha, \cos \alpha)$ .

The unit cell response was simulated in the frequency domain using a Floquet modal analysis. A transverse electromagnetic (TEM) mode with electric field parallel to  $y$  and normal incidence was used to excite the structure. The structure parameters  $w_x, w_y, d_x, d_y$  were optimized to get the maximum possible phase excursion of the reflection coefficient between the extreme cases of the LC permittivity while keeping at the same time the highest possible magnitude of the reflection coefficient in the operation band between 105 and 125 GHz. The LC layer thickness  $h_{LC}$  was fixed at a value of 40  $\mu\text{m}$  defined by the thickness of spacers available. As mentioned above, only the tensors corresponding to the LC substrate below the patch were rotated, assuming that only that area would be properly biased in the experimental demonstration.

Fig. 3 shows the amplitude and the phase of the reflection coefficient for different values of  $\alpha$  varying from 0 to 90°. As shown in Fig. 3(a), there is a resonant dip in the spectrum of the reflection coefficient magnitude which shifts from 117 to 108 GHz when the LC tensor is rotated from 0° to 90°. In all considered cases, its magnitude is above  $-2.5$  dB within the entire frequency band. This resonance is accompanied by a phase variation [Fig. 3(b)] which can be modulated by rotating the LC tensor. A maximum phase excursion of 266° is obtained at 113 GHz. To ease the comparison, all the phase curves have been normalized in Fig. 3(c), by simply subtracting the phase of each case to that of the 0° state of the LC tensor. There, it can be appreciated clearly the range of phases achieved by rotating the permittivity tensor. These results provide a complete characterization of the reflection phase as a function of  $\alpha$  and confirm the necessity of working in the vicinity of a resonance to observe a significant phase excursion.

A beam steerer that operates in reflection can be designed by incorporating a phase variation into the metasurface, as described by the following equation:

$$\phi(x) = k_0 d_x (\sin(\theta_r) - \sin(\theta_i)) \quad (9)$$

where  $\theta_r$  is the desired reflection angle,  $\theta_i$  is the angle of incidence and  $\phi(x)$  is the phase of each column composing the RA, achieved by rotating  $\alpha$ . Note that a modulation of the RA phase can only be achieved along the  $x$  axis since the columns are electrically connected and share the same biasing voltage.

For the numerical analysis, a single row consisting of  $1 \times 33$  unit cells was considered, with periodic boundary conditions applied along the  $y$ -direction (infinite in that direction) and open boundary conditions with an additional space (open+add space) along the  $x$ - and  $z$ -directions, as depicted in Fig. 4(a). The structure was illuminated by a plane wave with  $E_y$  transversal electric (TE) polarization with an incidence angle of  $\theta_i = 10$  deg. Fig. 4(b) displays the calculated radar cross section far-field patterns for the cases under consideration, at the frequency where the deflected peak has its maximum amplitude (refer to label). Fig. 4(c)-(f) presents 1D cuts at various frequencies, illustrating different output angles (from 20° to 35°). Through this analysis, it becomes evident that the deflected peaks can be observed at the primary frequency, alongside the presence of a specular beam at 10°. The cross-polar response is above  $-60$  dB (it is not represented in the plot), indicating negligible influence on the overall performance. To enhance the clarity of this analysis, we have included contour plot diagrams representing the radar cross section far-field patterns as a function of frequency and angle when the RA is configured to produce a reflected beam at 20°, 25°, 30°, and 35°, respectively, as depicted in Fig. 4(g)-(j). As shown there, in all cases the main reflection beam occurs at 10° (that corresponds to the specular reflection) in all the considered bandwidth except at the operation band wherein the RA is able to deflect the beam towards the desired direction (as indicated by the dashed lines).

### III. PROTOTYPE FABRICATION AND CHARACTERIZATION

To corroborate experimentally the previous results, the designed RA prototype was fabricated and measured. The prototype contains  $29 \times 33$  unit cells with overall dimensions

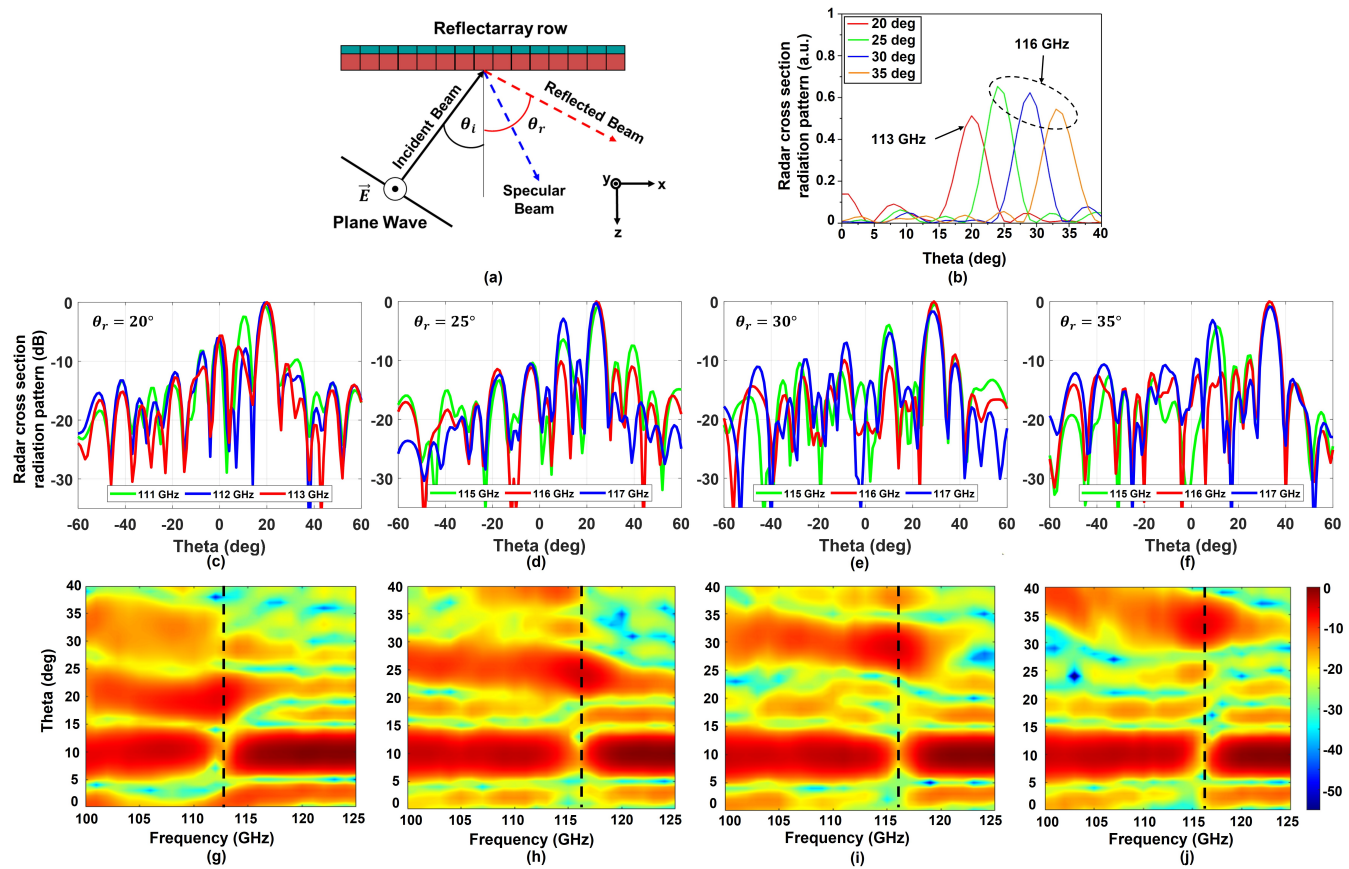


Fig. 4. (a) Beam-steerer simulation scenario where  $\theta_i = 10$  deg is the angle of the incident beam and  $\theta_r$  is the angle of the beam reflected in the desired direction. (b) Radar cross section far-field pattern at the frequency of maximum amplitude for the deflected peak (see label) for four different beam-steering cases. Radar cross section far-field pattern at different frequencies and for a beam reflected at (c) 20°, (d) 25°, (e) 30° and (f) 35°. Contour plot diagram for a beam reflected at (g) 20°, (h) 25°, (i) 30° and (j) 35°. Scale is in dB and each panel is normalized to the maximum.

of  $29.7 \times 30.45$  mm. Fig. 5(a) provides a detailed illustration of the biasing configuration used in the prototype. The 33 columns are connected to corresponding metallic pads to introduce the biasing voltage, thereby enabling proper operation of the LC.

The prototype was fabricated by preparing two polished round wafers made of fused quartz, with a diameter of 60 mm. The first wafer was 2 mm thick and was used for the MS, while the second was 6 mm thick and was used for the GP. Both wafers were symmetrically cut to a length of 13 cm, as shown in Fig. 5(a) and (b). This form of the quartz wafers was chosen to facilitate electric connection to the GP electrode after assembly. The experimental characterization of the dielectric permittivity of quartz plates in the band of 0.1 to 1.6 THz was done using a custom-made terahertz time-domain spectrometer developed in the Institute of Automation and Electrometry SB RAS (Novosibirsk, Russia) [25]. The material parameters and the thickness of the samples were retrieved from their THz spectra by means of the extraction method described in [26]. The properties of the quartz at these frequencies are really stable, showing a permittivity around 3.79 to 3.82 in the frequency range of 100 to 150 GHz [27]–[29]. Moreover, the loss tangent of the quartz is  $\leq 0.001$ , which indicates an excellent behavior of this material with a low

impact on the losses proposed structure. The wafers were then metallized on one surface with  $0.4 \mu\text{m}$ -thick aluminum using magnetron sputtering. Contact photolithography was used to create the MS pattern on the 2 mm-thick quartz wafer, which included the active patch array and elongated contact pads for electric connection to individual biasing lines. To avoid narrow gaps between the pads, they were separated into two sets: 17 pads were placed on one side to control the odd biasing lines, while 16 pads were located on the opposite side to govern the even ones, as shown in Fig. 5(a) and (b).

After metallization and photolithography, the MS and GP faces of the wafers that were to come into contact with the LC were coated with thin poly(vinyl alcohol) orienting layers using a spin coater (HO-TH-05, Holmarc, India). The orienting layers were then aligned by gently rubbing them with a rubbing machine (HO-IAD-BTR-01, Holmarc, India), ensuring that the unbiased LC molecules were aligned along the  $y$  axis on the wafer surface. The LC was then injected into the gap between the quartz wafers, which were separated by  $40 \mu\text{m}$ -thick polypropylene strip spacers. Finally, the edges were sealed to prevent LC leakage and ensure proper consolidation.

After completing fabrication of the “quartz-LC” core of the device, an auxiliary printed circuit board (PCB) was implemented to simplify the biasing connections, see Fig. 5.

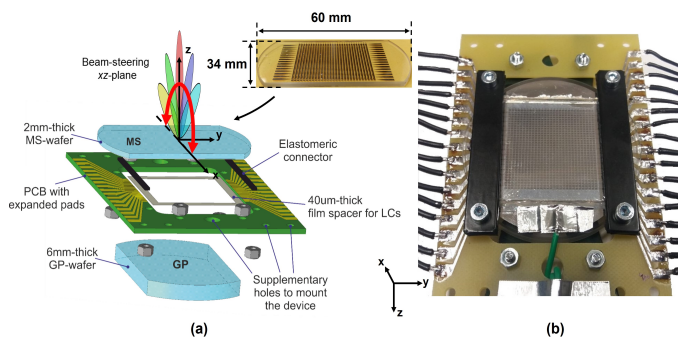


Fig. 5. Schematic representation of the manufactured RA: (a) Isometric exploded view of all the pieces composing the RA and showing in the center the PCB used to realize the bias connection. Inset, front view of the 2-mm-thick quartz wafer with active patches (MS) and contact pads, which has a size of 34 mm by 60 mm. (b) Photo of the assembled device prepared for connection to a 33-channel voltage generator.

The electric connection between pads on the quartz wafer and PCB was done using elastomeric connectors [30]. This type of flexible connectors, well-known in LC display technologies, is made as a set of narrow conductive layers interleaved with insulating ones. With elastomeric connectors the soldering process on the quartz wafers is avoided, preserving integrity of the LC device. Fig. 5(b) shows the final structure after assembling. Notice that soldering joints are located on the PCB outside the RA. The ground connection is provided through the green wire which is attached to the GP electrode by means of a metal foil sticky tape.

For the characterization of the fabricated RA, a Vector Network Analyzer (MVNA-8-350, AB Millimetre) was used, equipped with a quasi-optical bench and rotary platform. The samples were measured in the frequency range of 105-125 GHz with a step of 50 MHz. A horn antenna was used to transmit the wave, which was then focused on the sample by a pair of elliptical mirrors (see inset in Fig. 6(a)). In the first set of experiments, all biasing lines were driven at the same voltage, so the reflected wave traveled in the normal direction (since there was no phase difference among the unit cells). The reflected wave was then detected by the horn antenna, guided by the elliptical mirrors, and steered to the detector through a directional coupler connected to the antenna. Before performing the characterization, the setup was calibrated by placing a mirror in the sample position. The biasing voltage was varied from 0 V to 10 V in increments of 0.50 V, but for clarity, the curves are presented with a step of 1 V.

Fig. 6(a) presents the measured reflection coefficient magnitude. The losses obtained in the measurements are comparable to those obtained in the simulation, with a minimum reflection coefficient around 2.5 dB. A shift in frequency towards higher frequencies with respect to simulation results was observed, especially near the maximum bias state. The maximum experimental phase deviation was 210°, which is 56° lower than the simulation results, as seen in Fig. 6(b) and (c). There is also an abrupt change in phase between 1 V (light green curve) and 2 V (dark blue curve), indicating that the LC molecules have maximal sensitivity in this region and a small variation in biasing voltage yields substantial changes in LC director

orientation. Despite these differences, the experimental results validate the simulation, the good performance of the LC, and the correct bias connection implemented in the prototype. These results give a complete characterization of the reflection phase with a uniform bias voltage.

In the second set of experiments, a non-uniform biasing was applied to the RA. The experimental setup consisted of two horn antennas (working in *D*-band from 105 to 125 GHz) and a sample holder where the RA was placed. The sample holder was positioned on a rotary platform to control the angle of incidence and the receiving antenna was placed on a platform connected to the rotary platform to freely rotate and scan the angular power distribution. The experimental setup was covered with absorbing resin to minimize ambient reflections and a 33-channel voltage generator was used to independently feed all the biasing lines of the RA. All the setup implemented for this second experiment is illustrated in Fig. 7(a).

To further characterize the beam steering performance of the device, the incidence angle between the transmitter and the RA was fixed at 10 degrees. The biasing of the RA unit cells was properly controlled by adjusting the voltage generator to achieve the desired angle of reflection. It is important to note that the quantitative measurements of the device do not directly align with the simulation results, specifically the far-field pattern analysis. In this case, the measurement was focused on analyzing the transmission coefficient using the secondary horn antenna positioned at the reception location. Although there are quantitative differences between the measurements and simulations, the qualitative agreement is valid. The transmission coefficient peak should correspond to the analyzed output direction in simulations. Fig. 7(b), shows the transmission coefficient for different frequencies when the RA is configured to get a beam at 20°, 25°, 30° and 35°. Notice, that the number of analysis points along the *x*-axis is relatively fewer but sufficient to provide valuable insights. The presence of the specular beam at  $\theta = 10^\circ$  is clearly evident and significantly influences the quality of the beam at lower beam-steered angles. For a better understanding, Fig. 7(c) shows the contour plots analysis for a larger range of frequencies. Both studies, the 1D cuts and the contour plot analysis, demonstrated that for larger angles, the definition of the beam improves, thereby validating our experiment.

Beyond that, analysis of Fig. 7(b) and (c), specifically to  $\theta_r = 20^\circ$ , reveals that the device exhibits good pointing performance over a wide bandwidth, from 105 to 120 GHz, thus validating the correct biasing and confirming the results of the simulation. However, at  $\theta_r = 25^\circ$ , the bandwidth is reduced compared to the previous result, and the beam resolution is not as high. Nevertheless, the outcomes for the other angles demonstrate good behavior, displaying adequate beam pointing in the intended direction and retaining a sufficient bandwidth, which in most cases extends from 105 to 120 GHz.

Table. II provides a comprehensive comparison of our device with similar prototypes described in the literature. The analysis primarily focuses on key parameters such as losses, achieved phase shift, and scan angle. The devices evaluated work at different frequencies to present a comprehensive view of this technology. Our reconfigurable antenna (RA) stands

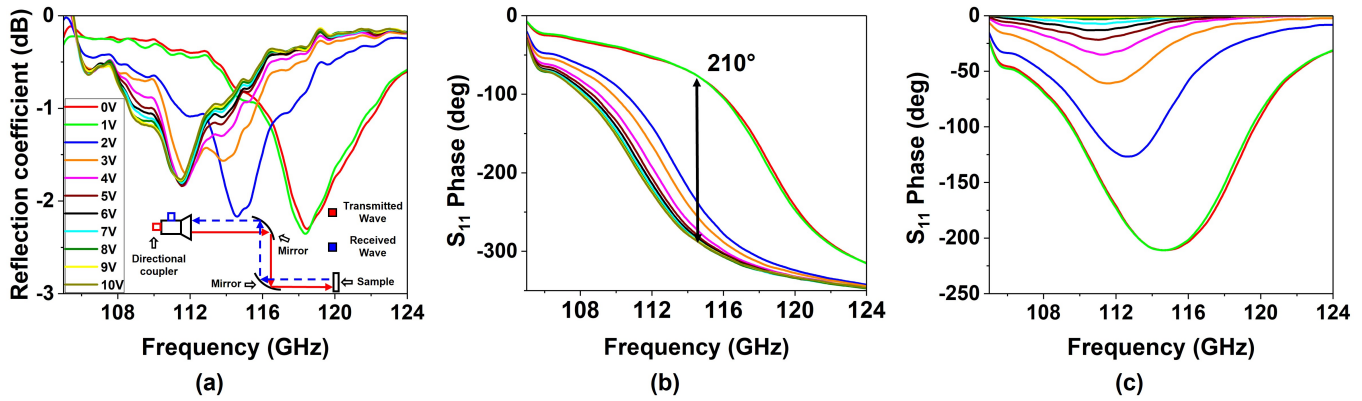


Fig. 6. (a) Reflection coefficient magnitude in dB. (b) Reflection phase in degrees. (c) Phase curves normalized to the case of 0V. (Inset) Setup employed in the characterization

TABLE II  
COMPARISON OF ELECTRICAL PERFORMANCE OF LC-REFLECTARRAYS.

Ref.	Frequency (GHz)	Size	Losses (dB)	Phase Shift	Scan angle
[31]	8.5-10	1 × 2	1.5	240°	-
[32]	28.5	10 × 10	14	290°	45°
[33]	96-104	54 × 54	7	300°	55°
[34]	114.9	30 × 30	13	189.2°	-
This paper	105-125	29 × 33	2.5	210°	35°

out due to its remarkably low losses, offering a balanced combination of fabrication simplicity, precise phase control, and moderate bandwidth. This achievement is made possible by harnessing the advantages of the new LC composition. However, it is important to note that further testing and optimization of this novel LC composition are necessary to fully exploit its capabilities.

Compared to previous works [31]–[33], our device has the potential for improved phase shift and, consequently, an increased scan angle. Despite this, the obtained low losses are a significant advancement, showcasing a nearly 5 dB reduction compared to other devices operating at the same frequency. These results underscore the immense technological potential of LC crystals in reconfigurable devices operating on millimeter waves.

#### IV. CONCLUSION

In this study, a reconfigurable LC-loaded reflectarray operating near 110 GHz was designed, fabricated, and experimentally evaluated. The device was configured as a high-impedance surface with a patch meta-array patterned on a 2 mm-thick quartz substrate separated from the ground plane by a 40 μm-thick LC layer. The electrical biasing of the LC-loaded RA unit cells was achieved by the addition of narrow inductive strips connecting adjacent patches in one dimension. The simulations indicated a maximum phase excursion of 266° with losses below 3 dB. In the 1D beam steering scenario, when properly tuned, the reflected beam was directed towards the desired direction at the operating frequency. The fabricated prototype with 29 × 33 unit cells exhibited a maximum phase

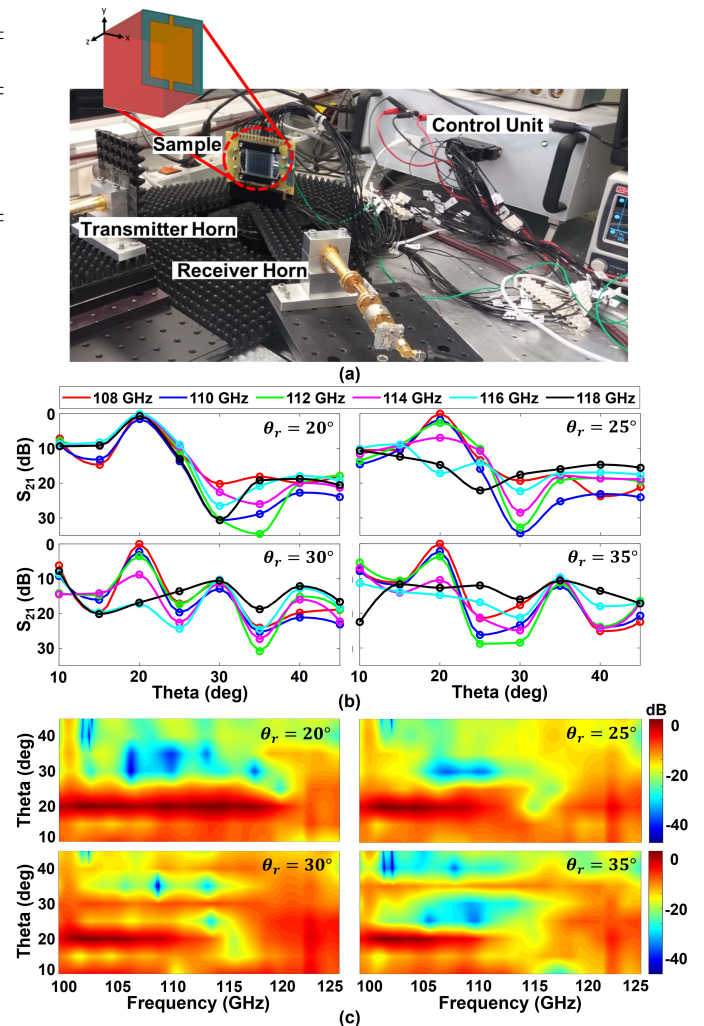


Fig. 7. (a) Photograph of the measurement scenario composed of two horn antennas and a rotating positioner where the RA under test is placed. Contour plot diagram for a reflected beam: (b) Transmission coefficient for different frequencies and reflected beams at  $\theta_r=20^\circ$ ,  $\theta_r=25^\circ$ ,  $\theta_r=30^\circ$  and  $\theta_r=35^\circ$ , (c) Contour plot diagram for the same reflected beams. Scale is in dB and each panel is normalized to the maximum.



excursion of 210° with losses around 2.5 dB. The experimental results demonstrated the capability of the device to steer the beam in the desired direction with a good pointing in a bandwidth of around 12 GHz. These results demonstrate the viability of LC technology for reconfigurable devices operating at millimeter and submillimeter waves, providing simple solutions for new applications.

## APPENDIX

### A. Developed Liquid Crystal Composition

Among the most promising liquid crystal compounds for high-frequency applications are nematic compositions based on polycyclic substances, particularly derivatives of n-quaterphenyl and n-quinquiphenyl with varying terminal (R, R') and lateral (A, B, C, D, E) substituents [23], [35], [36]. These substances can be represented by the general structural formulas presented in Table. III. Compared to 2- and 3-ring compounds, 4- and 5-ring LC compounds possess higher optical anisotropy, making them suitable for tunable LC devices. Additionally, the incorporation of lateral substituents into the ring molecules decreases their melting point and enhances miscibility.

In our study, we introduced innovative techniques for the synthesis of liquid-crystalline polyaromatic derivatives of n-quaterphenyl\* and n-quinquiphenyl\* with lateral substitution. Our methods utilize condensation processes to create substituted cyclic fragments, as reported in [35], [36]. They stand out for their ease of implementation, straightforwardness, and readily available starting materials. Our developed technology enables the synthesis of new polyaromatic LC compounds with exceptional optical anisotropy ( $\Delta n \geq 0.4$ , where  $\Delta n$  is the refractive index difference between ordinary and extraordinary axes) and robust chemical and photochemical stability. Most of the synthesized substances have a melting point below +80 to +90°C (for the best n-quaterphenyl\* compound it is even below +65°C) and the transition temperature to the isotropic state is less than 210°C. The synthesized LC compounds possess rod-shaped molecules and exhibit good solubility in most organic solvents and compatibility with low-viscosity LC compounds.

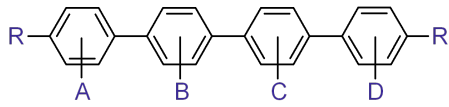
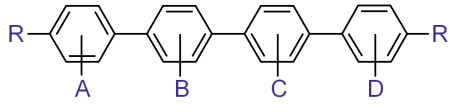
Based on the synthesized LC compounds, we have optimized and produced a promising LC composition for use in tunable meta-devices at both microwaves and millimeter waves. This composition, referred to as LCM-1, stands out for its low dielectric loss ( $< 0.003$ ), high dielectric anisotropy ( $> 1.3$ ) and low dispersion when compared to similar products.

The results obtained allow us to draw the following conclusions [23], [35], [36]: (i) The value of the birefringence of the LC molecule is a significant parameter but it is not the main factor that influences dielectric anisotropy in the high-frequency region; (ii) the bulk and type of polar groups have a substantial impact on the dielectric anisotropy; (iii) the presence of bridge fragments in the LC molecules reduces dielectric anisotropy at high frequencies.

### B. Design Guidelines

Here we summarize the design guidelines followed to implement the LC RA here reported. The design process started

TABLE III  
COMPONENTS OF THE DEVELOPED LC COMPOSITION LCM-1.

Substances	
n-quaterphenyl*	
n-quinquiphenyl*	

\*Substituents: R, R' = alkyl, F, NCS; A, B, C, D, E = Cl, CH<sub>3</sub>.

by choosing the unit cell which in this case is a rectangular patch resonator. It was chosen for simplicity both in design and manufacturing. In the initial design stage, the LC permittivity tensor values were extrapolated from measurements done in the microwave band [23], due to the difficulty to characterize it properly in the millimeter-wave range. The response of the structure was obtained performing unit cell analysis with a commercial electromagnetic solver. After these initial calculations, the device was manufactured and assembled, as described in the main text. Subsequently, an experimental characterization of the device's response was carried out, utilizing a uniform biasing voltage across all unit cells while systematically varying the bias voltage. This information was used in the next stage to adjust the permittivity tensor values and match the experimental reflectance data with the numerical simulator. These adjusted values were then utilized in all simulations presented within this manuscript, ensuring the consistency and accuracy of our results.

## ACKNOWLEDGMENT

This work was funded by Project RTI2018-094475-B-I00 funded by MCIN/ AEI /10.13039/501100011033/ FEDER “Una manera de hacer Europa”; S.A.K. acknowledges support from the Ministry of Science and Higher Education of the Russian Federation, grant 075-15-2020-797 (13.1902.21.0024). The authors also thank the Shared Equipment Center “Spectroscopy and Optics” of the Institute of Automation and Electrometry SB RAS for THz-TDS characterization of quartz wafers.

## REFERENCES

- [1] H. Zhang, X. Chen, Z. Wang, Y. Ge, and J. Pu, “A 1-Bit Electronically Reconfigurable Reflectarray Antenna in X Band,” *IEEE Access*, vol. 7, pp. 66567–66575, 2019.
- [2] Z. Wang, Y. Ge, J. Pu, X. Chen, G. Li, Y. Wang, K. Liu, H. Zhang, and Z. Chen, “1 Bit Electronically Reconfigurable Folded Reflectarray Antenna Based on p-i-n Diodes for Wide-Angle Beam-Scanning Applications,” *IEEE Transactions on Antennas and Propagation*, vol. 68, pp. 6806–6810, sep 2020.
- [3] Chih-Chieh Cheng and A. Abbaspour-Tamijani, “Evaluation of a Novel Topology for MEMS Programmable Reflectarray Antennas,” *IEEE Transactions on Microwave Theory and Techniques*, vol. 57, pp. 3333–3344, dec 2009.
- [4] O. Bayraktar, O. A. Civi, and T. Akin, “Beam switching reflectarray monolithically integrated with RF MEMS switches,” *IEEE Transactions on Antennas and Propagation*, vol. 60, no. 2 PART 2, pp. 854–862, 2012.

- [5] G. Perez-Palomino, J. Encinar, M. Barba, and E. Carrasco, "Design and evaluation of multi-resonant unit cells based on liquid crystals for reconfigurable reflectarrays," *IET Microwaves, Antennas & Propagation*, vol. 6, no. 3, p. 348, 2012.
- [6] S. C. Pavone, E. Martini, F. Caminita, M. Albani, and S. Maci, "Surface Wave Dispersion for a Tunable Grounded Liquid Crystal Substrate Without and With Metasurface on Top," *IEEE Transactions on Antennas and Propagation*, vol. 65, pp. 3540–3548, jul 2017.
- [7] E. Martini, S. C. Pavone, M. Albani, S. Maci, V. Martorelli, G. Giodanengo, A. Ferraro, R. Beccherelli, G. Toso, and G. Vecchi, "Reconfigurable antenna based on liquid crystals for continuous beam scanning with a single control," *2019 IEEE International Symposium on Antennas and Propagation and USNC-URSI Radio Science Meeting, APSURSI 2019 - Proceedings*, no. 4000114502, pp. 449–450, 2019.
- [8] K. Lu, "Spatial Phase Modulator," *Optical Engineering*, vol. 29, no. 3, pp. 240–246, 1990.
- [9] M. Sharma, N. Hendler, and T. Ellenbogen, "Electrically Switchable Color Tags Based on Active Liquid-Crystal Plasmonic Metasurface Platform," *Advanced Optical Materials*, vol. 8, p. 1901182, apr 2020.
- [10] M. Ismail and A. Zain, "Phase tunability of reflectarray patch elements using tunable dielectric substrate of nematic liquid crystal," in *2009 IEEE International Workshop on Antenna Technology*, no. 1, pp. 1–4, IEEE, mar 2009.
- [11] R. Guirado, G. Perez-Palomino, M. Ferreras, E. Carrasco, and M. Cano-Garcia, "Dynamic Modelling of Liquid Crystal-Based Metasurfaces and its Application to Reducing Reconfigurability Times," *IEEE Transactions on Antennas and Propagation*, vol. 70, no. 12, pp. 1–1, 2022.
- [12] J. Wu, Z. Shen, S. Ge, B. Chen, Z. Shen, T. Wang, C. Zhang, W. Hu, K. Fan, W. Padilla, Y. Lu, B. Jin, J. Chen, and P. Wu, "Liquid crystal programmable metasurface for terahertz beam steering," *Applied Physics Letters*, vol. 116, 3 2020.
- [13] R. Stevenson, M. Sazegar, A. Bily, M. Johnson, and N. Kundtz, "Metamaterial surface antenna technology: Commercialization through diffractive metamaterials and liquid crystal display manufacturing," *2016 10th International Congress on Advanced Electromagnetic Materials in Microwaves and Optics, METAMATERIALS 2016*, no. September, pp. 349–351, 2016.
- [14] W. Hu, R. Dickie, R. Cahill, H. Gamble, Y. Ismail, V. Fusco, D. Linton, N. Grant, and S. Rea, "Liquid Crystal Tunable mm Wave Frequency Selective Surface," *IEEE Microwave and Wireless Components Letters*, vol. 17, pp. 667–669, sep 2007.
- [15] G. Perez-Palomino, P. Baine, R. Dickie, M. Bain, J. A. Encinar, R. Cahill, M. Barba, and G. Toso, "Design and Experimental Validation of Liquid Crystal-Based Reconfigurable Reflectarray Elements With Improved Bandwidth in F-Band," *IEEE Transactions on Antennas and Propagation*, vol. 61, pp. 1704–1713, apr 2013.
- [16] W. Hu, R. Cahill, J. A. Encinar, R. Dickie, H. Gamble, V. Fusco, and N. Grant, "Design and Measurement of Reconfigurable Millimeter Wave Reflectarray Cells With Nematic Liquid Crystal," *IEEE Transactions on Antennas and Propagation*, vol. 56, pp. 3112–3117, oct 2008.
- [17] S. A. Kuznetsov, A. G. Paulish, M. Navarro-Cía, and A. V. Arzhannikov, "Selective Pyroelectric Detection of Millimetre Waves Using Ultra-Thin Metasurface Absorbers," *Scientific Reports*, vol. 6, p. 21079, feb 2016.
- [18] Suparyanto dan Rosad (2015), *Metamaterials*, vol. 5. Hoboken, NJ, USA: John Wiley & Sons, Inc., may 2006.
- [19] D. M. Pozar, *Microwave Engineering*. John Wiley & Sons, Inc., 4th ed. ed., 2011.
- [20] F. Costa, S. Genovesi, and A. Monorchio, "On the Bandwidth of High-Impedance Frequency Selective Surfaces," *IEEE Antennas and Wireless Propagation Letters*, vol. 8, pp. 1341–1344, 2009.
- [21] (2023). CST STUDIO SUITE.®, "[Online]. Available: <https://www.3ds.com/products-services/simulia/products/cst-studio-suite>."
- [22] J. A. Encinar, M. Arrebola, L. F. De La Fuente, and G. Toso, "A transmit-receive reflectarray antenna for direct broadcast satellite applications," *IEEE Transactions on Antennas and Propagation*, vol. 59, no. 9, pp. 3255–3264, 2011.
- [23] V. Lapanik, G. Sasnouski, S. Timofeev, E. Shepeleva, G. Evtushkin, and W. Haase, "New highly anisotropic liquid crystal materials for high-frequency applications," *Liquid Crystals*, vol. 45, pp. 1242–1249, jun 2018.
- [24] N. Koide, *The Liquid Crystal Display Story*. Tokyo: Springer Japan, 2014.
- [25] I. Jáuregui-López, P. Rodríguez-Ulbarri, S. A. Kuznetsov, N. A. Nikolaev, and M. Beruete, "Thz sensing with anomalous extraordinary optical transmission hole arrays," *Sensors (Switzerland)*, vol. 18, 11 2018.
- [26] L. Duvillaret, F. Garet, and J.-L. Coutaz, "A reliable method for extraction of material parameters in terahertz time-domain spectroscopy," 1996.
- [27] E. A. Serov, V. V. Parshin, K. V. Vlasova, and A. I. Makarov, "Modern dielectric materials for output windows of high-power microwave and terahertz sources," *Journal of Infrared, Millimeter, and Terahertz Waves*, vol. 41, pp. 1450–1459, 12 2020.
- [28] M. Naftaly and A. Gregory, "Terahertz and microwave optical properties of single-crystal quartz and vitreous silica and the behavior of the boson peak," *Applied Sciences*, vol. 11, p. 6733, 7 2021.
- [29] J. W. Lamb, "Miscellaneous data on materials for millimetre and submillimetre optics," 1996.
- [30] ZEBRA® Elastomeric Connectors, "ZEBRA® Elastomeric Connectors."
- [31] H. Kim, J. Kim, and J. Oh, "Liquid-crystal-based  $\mu$ i;x/i;  $\mu$ i; -band reactively loaded reflectarray unit cell to reduce reflection loss," *IEEE Antennas and Wireless Propagation Letters*, vol. 20, pp. 1898–1902, 10 2021.
- [32] P. Aghabeyki, Y. Cai, G. Deng, Z.-H. Tan, and S. Zhang, "A dual-polarized reconfigurable reflectarray with a thin liquid crystal layer and 2-d beam scanning," *IEEE Transactions on Antennas and Propagation*, vol. 71, pp. 3282–3293, 4 2023.
- [33] G. Perez-Palomino, M. Barba, J. A. Encinar, R. Cahill, R. Dickie, P. Baine, and M. Bain, "Design and demonstration of an electronically scanned reflectarray antenna at 100 ghz using multiresonant cells based on liquid crystals," *IEEE Transactions on Antennas and Propagation*, vol. 63, pp. 3722–3727, 8 2015.
- [34] J. Yang, X. Chu, H. Gao, P. Wang, G. Deng, Z. Yin, and H. Lu, "Fully Electronically Phase Modulation of Millimeter-Wave via Comb Electrodes and Liquid Crystal," *IEEE Antennas and Wireless Propagation Letters*, vol. 20, pp. 342–345, mar 2021.
- [35] G. Sasnouski, V. Lapanik, R. Dabrowski, and J. Dziaduszek, "Synthesis of new LC compounds with high optical anisotropy: pentaphenyl derivatives lateral substituted," *Phase Transitions*, vol. 85, pp. 309–313, apr 2012.
- [36] G. Sasnouski, V. Lapanik, V. Bezborodov, R. Dabrowski, and J. Dziaduszek, "Synthesis of fluoro substituted quaterphenyl liquid crystals," *Phase Transitions*, vol. 87, pp. 783–789, aug 2014.



**Dayan Pérez-Quintana** was born in Cuba in 1991. He received the M.Sc. degree in telecommunication engineering from the Instituto Superior Politécnico José Antonio Echeverría (ISPJAE), Havana, Cuba, in 2015, and the Ph.D. degree in telecommunication engineering from the Public University of Navarra (UPNA), Pamplona, Spain, in 2022. During his Ph.D. studies, he spent three months as research stay with the School of Electrical Engineering and Computer Science (EECS), KTH Royal Institute of Technology, Stockholm, Sweden. He worked as a Pre-Doctoral Research Fellow with the Antenna Group, Electrical, Electronic and Communication Engineering Department, UPNA, from 2018 to 2022. Since 2023, he has been a Post-Doctoral Research Fellow with the Electromagnetics Group, University of Siena.

His research interests include millimeter-wave and THz components and antennas and metamaterials. Dr. Pérez-Quintana was a recipient of the Young Scientist Award at the 3rd Union Radio-Scientifique Internationale (URSI) Atlantic Radio Science Meeting (AT-AP-RASC) in 2022.

His research interests include millimeter-wave and THz components and antennas and metamaterials. Dr. Pérez-Quintana was a recipient of the Young Scientist Award at the 3rd Union Radio-Scientifique Internationale (URSI) Atlantic Radio Science Meeting (AT-AP-RASC) in 2022.



**Erik Aguirre** received his MSc in Telecommunications Engineering from the Public University of Navarra, in 2012. He obtained the Ph.D degree in 2014. From 2012 to 2014 he worked in a research project at University of Vigo related to dispersive propagation. Since 2015 he has been working in Tafco Metawireless. From 2016 he is Assistant Lecturer at UPNA. His research interests include radio propagation in dispersive media, body-centric communications, and wireless sensor networks.



**Eduardo Olariaga** received his MSc in Telecommunications Engineering from the Polytechnic University of Catalonia, in 1992. In 1993 he was awarded with a two-years grant for the development of research projects at the Ikerlan Technology Center. In 1995 he was hired as Assistant Lecturer at Public University of Navarre. From 1995 to 1999 he worked as automation engineer in a dairy sector company. From 2000 to 2010 he worked in companies linked to Home Automation sector, occupying different positions such as Product Manager, Product Development

Project Manager and becoming responsible for the Home Automation Department. He obtained the Master on Business Administration in 2006. Since 2011 he has been working in Tafco Metawireless. His current research interests include microwave communications devices and wireless sensor networks.



**Vitaly Sutormin** graduated from Siberian Federal University, Russia, in 2010. After that he joined the molecular spectroscopy laboratory at Kirensky Institute of Physics, Russia, and received his Ph.D. in physics and mathematics in 2014. The theme of his thesis was “Electrooptical properties of liquid crystal cells with ionic-surfactant control method”. His research interest includes optics of liquid crystals.



**Victor Zyryanov** graduated from optics in the Department of Physics at Krasnoyarsk State University, Russia, in 1977. After that he joined Kirensky Institute of Physics, Russia, and received his Ph.D. in 1988 and Doctor of Sciences (Rus.) in physics and mathematics in 2002. The theme of his thesis was “Structural, optical, and electrooptical properties of uniaxially oriented films of polymer-dispersed liquid crystals”. He is currently the head of laboratory of molecular spectroscopy at Kirensky Institute of Physics.



**Jose A. Marcotegui** was born in Pamplona (Navarra), Spain in 1966. In 1992 he finished his studies in Telecommunications Engineering at the Polytechnic University of Catalonia. In 2017 he obtained a Ph.D. degree within the Communications Technologies program at the Public University of Navarre. I started my professional career in 1993 in the company Sistemas Navarra S.A. as a project engineer. In 1996 he created the company Conatel S.L. and he was hired as an associate professor at the Public University of Navarre. He remained as

an associate professor until 2009. In 2008 he founded the company Tafco Metawireless S.L. together with Professor Mario Sorolla Ayza and Professor Francisco Falcone. He is currently still working at Tafco Metawireless S.L., and he is responsible for R&D of the company.



**Miguel Beruete** received the M.Sc. and Ph.D. degrees in telecommunication engineering from the Public University of Navarre (UPNA), Pamplona, Spain, in 2002 and 2006, respectively.

From 2007 to 2009, he was with the Electronics Department, Technological Center CEMITEC, Noain, Navarra, Spain. In 2009, he joined TERALAB, Pamplona, Navarra, UPNA, as a Post-Doctoral Researcher of the Consolider EMET Engineering Metamaterials Project. From 2012 to 2016, he was a Ramon y Cajal Fellow Researcher and in 2017, he was appointed a UPNA Distinguished Researcher. Since 2017, he has been an Associate Professor at UPNA, where he leads the TERALAB Laboratory. In 2018, he became a Group Leader at the Multispectral Biosensing Group, Navarrabiomed, Pamplona. He has authored more than 160 indexed articles, five book chapters, and near 400 conference communications (several invited). He holds three patents and has participated in more than 70 research projects/contracts (Principal Investigator (PI) in 23) of international, national, and regional funding. He is a reviewer for more than 50 international journals. His current research interests include metasurfaces and metamaterials for infrared applications (radiative cooling and camouflage) and millimeter/terahertz-wave communication technologies.

Dr. Beruete has been included in the Stanford University's list of the top 2% most-cited scientists since the first edition (2020, 2021, 2022, 2023), was awarded with the Ph.D. Prize from UPNA for the Best Doctoral Thesis (2006–2007), the Research Prize UPNA for the best scientific contribution (2017–2018), three CST University Publication awards (2005, 2012, and 2016), the XII Talgo Award of Technological Innovation in 2011, and several awards of international conferences.